Supporting Information for Ultralow Thermal Conductivity and Mechanical Resilience of Architected Nanolattices

Nicholas G. Dou,[†] Robert A. Jagt,[†,‡] Carlos M. Portela,[†] Julia R. Greer,[†] and Austin J. Minnich[*,†]

[†]*Division of Engineering and Applied Science, California Institute of Technology, Pasadena, California 91125, United States*

[‡]*Faculty of Science and Engineering, University of Groningen, 9747 AG Groningen, The Netherlands*

E-mail: aminnich@caltech.edu

Sample fabrication

To create hollow alumina nanolattice samples suitable for the 3ω experiment, we augment the general fabrication process outlined by Meza et al.[1] The procedure begins by creating an octet-truss polymer scaffold using a two-photon lithography direct laser write process. We use the Photonic Professional system (Nanoscribe GmbH) with the proprietary IP-Dip photoresist. The Nanoscribe system incorporates a mirror galvanometer that enables rapid in-plane rastering and reduces the write time for this millimeter-length structure to a few hours. The structures are developed using propylene glycol methyl ether acetate and isopropyl alcohol.

A highly conformal layer of amorphous aluminum oxide is coated onto this polymer scaffold using a Savannah atomic layer deposition (ALD) system (Cambridge Nanotech). One ALD cycle consists of pulsing trimethylaluminum for 0.015 s, purging for 20 s, pulsing water for 0.015 s, and purging again for 20 s. The deposition chamber is held at 150 °C as 20 sccm of N_2 carrier gas is flowed through continuously. This ALD recipe produces self-limited growth of Al_2O_3 at a rate of 1.07 Å per cycle. Film thickness measurements taken with an alpha-SE ellipsometer (J. A. Woollam Co.) confirm the accuracy of the recipe deposition rate to within 1 percent. The resulting nanolattice has beams with a polymer core encapsulated by an alumina shell.

We then remove the polymer inside the beams by milling away sacrificial beams with a focused ion beam (FIB) and etching away the polymer through these openings with oxygen plasma. The FIBs are part of larger Nova 200/600 NanoLab systems (FEI Co.) and the plasma asher is a Zepto unit (Diener electronic GmbH). To expedite complete removal of the polymer, we write sacrificial beams at the vertical center of the structure so that the longest diffusion paths to the top and bottom are minimized. All samples are etched for at least 36 hours with 100 W of power and the structures are inspected afterwards under a scanning electron microscope to check for a contrast change indicating that the beams are hollow.

Finally, we deposit gold through an aligned shadow mask to create a continuous heater

line on the structure connected to four contact pads on the substrate. The mask is laser cut from 0.005 in stainless steel and has maximum edge waviness less than 5 µm. It is suspended above the sample by a spacer to avoid damaging the nanolattice and aligned under an optical microscope using micrometer-controlled translation stages. Thin film deposition is done in a LAB Line E-Beam evaporator (Kurt J. Lesker Co.) at pressures in the 10^{-7} Torr range. A 10 nm layer of titanium promotes adhesion of the 100 nm gold layer. The final position of the pattern deviates from the desired location by up to 10 µm due to imperfect alignment and non-normal evaporation through the mask, but precise positioning and edge sharpness are not critical for the experiment. Energy-dispersive x-ray spectroscopy shows negligible overspray of gold onto the sides of the nanolattices, confirming that evaporated gold does not contaminate the nanolattices.

Thermal experiments

3ω experiments are performed in a ST-100 cryostat (Janis Research Co.) at temperatures from 95 to 300 K and pressures in the 10^{-6} Torr range. A 6221 current source (Keithley Instruments) supplies power and an SR830 lock-in amplifier (Stanford Research Systems Inc.) measures voltages. In each experiment, we tune input power in the 4 to 40 µW range to ensure that the temperature rise at the heater line is less than 1 K. The thermal frequency response is measured from 1 to 1000 Hz by averaging 30 samples at each frequency.

To interpret the experimental data, we developed a custom thermal model described in the Supplementary Text. Our model accounts for lateral heat conduction through the gold heater line, 1-dimensional heat conduction through the alumina plate, and 2-dimensional heat conduction through the nanolattice and into the silicon substrate. The back side of the silicon chip is assumed to be isothermal. We use handbook values for density, specific heat, and thermal conductivity of silicon.[2] For amorphous alumina, we take the density to be 2900 kg m^{-3},[3] and the specific heat as the handbook value. The temperature-dependent ther-

mal conductivity of bulk amorphous alumina is taken from measurements of RF-sputtered alumina.[4] The heat capacities and effective thermal conductivities of the plate and nanolattice are further scaled by the calculated relative densities of the respective structures. For the gold heater line, we use a density of $18\,884\,\mathrm{kg\,m^{-3}}$,[5] and calculate thermal conductivity from electrical resistance via the Wiedemann-Franz law.

We extract thermal conductivity by performing a nonlinear least-squares fit on both the in-phase and out-of-phase components of the temperature response from 1 to 100 Hz. In this low frequency range, the thermal penetration depth is much longer than the height of the nanolattice. The fitting parameters are nanolattice thermal conductivity and a constant normalization factor.

Mechanical experiments and simulations

The uniaxial compression experiments provided stress-strain curves from which the Young's modulus and yield strength of each nanolattice was calculated. Several identical samples were compressed for each set of parameters that were used for the thermal samples. Specifically, all samples had an r/l ratio of 0.108, t/r ratios from 0.013 to 0.10, and spanned a relative density range from 0.78 to 4.1 %. The relative density values were calculated using a CAD model (SolidWorks), using dimensions obtained from SEM micrographs. Figure S3 depicts representative stress-strain curves for each geometry. Slight misalignments between the indenter tip and the top of the lattice commonly caused a non-linear regime upon first contact, followed by a linear loading regime, which transitioned into sequential or catastrophic failure (depending on the t/r ratio). For samples with wall thicknesses of 24 nm, several instabilities occurred within 20% strain increments, corresponding to a displacement equal to the unit cell height, indicating that shell buckling in struts was a significant deformation mechanism in addition to microcracking at nodes. Shell buckling is an elastic process that enables the recovery observed in Figure 3. Thicker-walled nanolattices exhibit fewer and more extensive

strain bursts that correspond to discrete fracture events, such as the collapse and densification of unit cell layers. Samples with wall thicknesses above 81 nm failed catastrophically. No recovery was observed for samples with wall thicknesses of 36 nm and above. In order to minimize the effects of initial misalignments between the lattices and the indenter, the maximum slope of the linear loading regime was taken as the measured Young's modulus. The effective strength was determined as the stress at the initial instability for recoverable samples or the maximum stress for samples that failed catastrophically.

Figure S4 shows the stiffness values of all fabricated samples compared to finite element simulations with identical parameters (Abaqus FEA). The simulations consisted of a discretized octet-truss unit cell composed of S3R shell elements and a linear elastic material model, where the Young's modulus and Poisson's ratio of ALD alumina were used.[6] Periodic boundary conditions (PBC) were applied on all sides of the unit cell, and a uniaxial strain was enforced as a linear perturbation. The simulation size ranged from 110 000 to 310 000 elements depending on the r/l and t/r parameters used.

The power-law fits of the form $E^* \propto \rho^m$ in Figure S4 yielded scaling exponents of $m = 1.41$ and 1.91 for simulations and experiments, respectively. The vertical offset and the higher scaling of the experimental samples in comparison to the defect-free simulations can be attributed to imperfections such as wall waviness (on the order of a few nanometers), which has been shown to significantly decrease the stiffness of thin-walled hollow beams.[7] The nonlinear scaling is consistent with the analysis done in that work, where the complex parameter space of hollow nanolattices is explained.

Figure S5 presents the Young's modulus and yield strength of the hollow alumina nanolattices in this work along with those reported for silica and carbon aerogels versus density. These plots demonstrate that nanolattices have more than an order of magnitude higher stiffness and strength at a given density. The nanolattices achieve similar stiffnesses and strengths as aerogels at half the density. This improvement in mechanical properties becomes even more pronounced at low densities because nanolattices have more favorable

density scalings. Compared to the stiffness scaling exponent for the nanolattice measurements, $m = 1.91$, the scaling exponents for silica and carbon aerogels are considerably higher, $m = 2.42$ and 3.20. Using a similar power-law model for strength, $\sigma_y \propto \rho^n$, the scaling exponent for our nanolattices is $n = 1.75$ while the density scaling for aerogels ranges from $n = 2.02$ to 2.97.

Prior to manufacturing the samples, PBC simulations with constant wall thickness and unit cell size but varying beam radius r were used to find an optimal r/l value at which the stiffness of circular-beam hollow octet-truss nanolattices was maximized. Figure S6 shows the resulting stiffness as r/l was varied from 0.014 to 0.14 and t/l remained at 0.007. The observed trend guided the design of the samples with $r/l \approx 0.1$.

3ω thermal model

3ω measurement samples for ultralow thermal conductivity materials typically consist of a slab or uniform film on a substrate with a metal heater line patterned on top.[4,8] In those cases, the heater line is thermally insulated from the heat sink. The nanolattice fabrication process prohibits us from creating macroscale structures, so we only construct the nanolattice directly underneath the heater line.

The nanolattice sample geometry leads to non-negligible heat loss through the metal heater line. This occurs because the heater line is connected to contact pads that lie directly on the substrate, which serves as the heat sink. The nanolattice thermal conductivity is so low that despite the small cross-sectional area of the metal line ($50\,\mu m \times 100\,nm$), the thermal resistance of the conduction path through the nanolattice is comparable to the thermal resistance through the metal line. Hence, the usual method of extracting thermal conductivity from a 3ω experiment does not work for our nanolattice samples, and we need to develop a thermal model that incorporates heat conduction along the heater line.

The following equations describe heat conduction through our nanolattice sample during

a 3ω experiment.

$$
\begin{cases}
\dfrac{\partial^2 T_i}{\partial y_i^2} + \lambda_i \dfrac{\partial^2 T_i}{\partial z^2} - \dfrac{1}{\alpha_i}\dfrac{\partial T_i}{\partial t} = 0 & \text{in} \quad 0 < y_i < d_i, \quad 0 < z < L & (1) \\
\dfrac{\kappa_1}{\kappa_0 d_0}\dfrac{\partial T_1}{\partial y_1} + \lambda_0 \dfrac{\partial^2 T_0}{\partial z^2} - \dfrac{1}{\alpha_0}\dfrac{\partial T_0}{\partial t} = -\dfrac{g}{\kappa_0} e^{j\omega t} & \text{on} \quad y_1 = 0 & (2) \\
\kappa_i \dfrac{\partial T_i}{\partial y_i} = \kappa_{i+1} \dfrac{\partial T_{i+1}}{\partial y_{i+1}} & \text{on} \quad y_i = d_i, \quad i = 1, \ldots, m-1 & (3) \\
T_i = T_{i+1} & \text{on} \quad y_i = d_i, \quad i = 0, \ldots, m-1 & (4) \\
T_m = 0 & \text{on} \quad y_m = d_m & (5) \\
T_i = 0 & \text{on} \quad z = 0, \quad z = L & (6)
\end{cases}
$$

In the equations above, z is the in-plane coordinate parallel to the heater line and y_i is the cross-plane coordinate, defined such that $y_i = d_i$ coincides with $y_{i+1} = 0$. Because the width of the heater line is identical to that of the nanolattice, we expect no temperature variation in the other in-plane direction x, perpendicular to the heater line. T_i, κ_i, λ_i, α_i, and d_i denote the temperature, cross-plane thermal conductivity, ratio of in-plane to cross-plane thermal conductivity, cross-plane thermal diffusivity, and thickness of the i-th layer, where $i = 0$ corresponds to the heater line. Instead of a prescribed surface heat flux, we impose a boundary condition that describes a thin skin of highly conductive material that generates heat (Equation 2).[9]

The general solution that satisfies the diffusion equation (Equation 1) and isothermal boundary conditions in z (Equation 6) can be expressed as a Fourier sine series. In layer i, the temperature and heat flux have the form

$$
T_i = e^{j\omega t} \sum_{n=1}^{\infty} \left(a_{in} \cosh q_{in} y_i + b_{in} \sinh q_{in} y_i \right) \sin \frac{n\pi z}{L} = e^{j\omega t} \sum_{n=1}^{\infty} T_{in} \sin \frac{n\pi z}{L} \tag{7}
$$

$$
Q_i = -e^{j\omega t} \sum_{n=1}^{\infty} \kappa_i q_{in} \left(a_{in} \sinh q_{in} y_i + b_{in} \cosh q_{in} y_i \right) \sin \frac{n\pi z}{L} = e^{j\omega t} \sum_{n=1}^{\infty} Q_{in} \sin \frac{n\pi z}{L} \tag{8}
$$

$$
q_{in}^2 = \lambda_i \left(\frac{n\pi}{L} \right)^2 + \frac{j\omega}{\alpha_i} \tag{9}
$$

The constants a_{in} and b_{in} are chosen to satisfy the boundary conditions in y_i. These can be solved using the transfer matrix method.[9]

$$\begin{pmatrix} T_{in} \\ Q_{in} \end{pmatrix}_{y_i \le d_i} = \begin{pmatrix} \cosh q_{in} y_i & -\frac{1}{\kappa_i q_{in}} \sinh q_{in} y_i \\ -\kappa_i q_{in} \sinh q_{in} y_i & \cosh q_{in} y_i \end{pmatrix} \begin{pmatrix} T_{in} \\ Q_{in} \end{pmatrix}_{y_i = 0} \tag{10}$$

By enforcing continuity of temperature and heat flux across layers (Equations 3 and 4), we can compose m of these matrices to relate T_{0n} and Q_{0n} at the heater line to T_{mn} and Q_{mn} at the isothermal surface.

$$\begin{aligned} \begin{pmatrix} T_{mn} \\ Q_{mn} \end{pmatrix}_{y_m = d_m} &= \begin{pmatrix} A_{mn} & B_{mn} \\ C_{mn} & D_{mn} \end{pmatrix} \cdots \begin{pmatrix} A_{1n} & B_{1n} \\ C_{1n} & D_{1n} \end{pmatrix} \begin{pmatrix} T_{1n} \\ Q_{1n} \end{pmatrix}_{y_1 = 0} \\ &= \begin{pmatrix} A_n & B_n \\ C_n & D_n \end{pmatrix} \begin{pmatrix} T_{1n} \\ Q_{1n} \end{pmatrix}_{y_1 = 0} \end{aligned} \tag{11}$$

Here, matrix elements are evaluated at $y_i = d_i$. The isothermal boundary condition $T_{mn} = 0$ (Equation 5) thus implies

$$T_{1n} = -\frac{B_n}{A_n} Q_{1n} = \frac{\gamma_n}{\kappa_0 q_{0n}} Q_{1n} \tag{12}$$

where we define the dimensionless quantity $\gamma_n = -\kappa_0 q_{0n} B_n / A_n$. The ratio B_n/A_n can be calculated using the algorithm given by Borca-Tasciuc et al.[10] Finally, the heater line boundary condition is used to obtain a_{1n} and b_{1n}, giving

$$T_1 = \frac{g d_0^2}{\kappa_0} e^{j\omega t} \sum_{n \text{ odd}} \frac{\gamma_n \cosh q_{1n} y_1 - \frac{\kappa_0 q_{0n}}{\kappa_1 q_{1n}} \sinh q_{1n} y_1}{\left(1 + \gamma_n q_{0n} d_0\right) q_{0n} d_0} \left(\frac{4}{n\pi} \sin \frac{n\pi z}{L} \right) \tag{13}$$

$$Q_1 = g d_0 e^{j\omega t} \sum_{n \text{ odd}} \frac{\cosh q_{1n} y_1 - \gamma_n \frac{\kappa_1 q_{1n}}{\kappa_0 q_{0n}} \sinh q_{1n} y_1}{1 + \gamma_n q_{0n} d_0} \left(\frac{4}{n\pi} \sin \frac{n\pi z}{L} \right) \tag{14}$$

Note that the sum is evaluated only over odd natural numbers. Because hyperbolic cosine and sine grow rapidly, it is more numerically stable to evaluate the temperature and heat

flux using exponentials. For example,

$$T_1 = \frac{gd_0^2}{\kappa_0} e^{j\omega t} \sum_{n\,\text{odd}} \frac{c_{1n} e^{q_{1n} y_1} + d_{1n} e^{-q_{1n} y_1}}{(1 + \gamma_n q_{0n} d_0)\, q_{0n} d_0} \left(\frac{4}{n\pi} \sin \frac{n\pi z}{L} \right) \tag{15}$$

$$c_{1n} = \frac{1}{2} \left(\gamma_n - \frac{\kappa_0 q_{0n}}{\kappa_1 q_{1n}} \right) \tag{16}$$

$$d_{1n} = \frac{1}{2} \left(\gamma_n + \frac{\kappa_0 q_{0n}}{\kappa_1 q_{1n}} \right) \tag{17}$$

Figure S1 shows an example temperature and heat flux field for a single layer.

In the 3ω experiment, the measured voltage is directly related to the average heater line temperature, given by evaluating Equation 13 at $y_1 = 0$ and integrating with respect to z. The resulting thermal frequency response is

$$T_\omega = \frac{gd_0^2}{\kappa_0} \sum_{n\,\text{odd}} \frac{8\gamma_n}{n^2\pi^2 (1 + \gamma_n q_{0n} d_0)\, q_{0n} d_0} \tag{18}$$

Critical t/r and r/l ratios

Following the analysis done by Meza et al.,[1] the dominating deformation modes for circular cross-section hollow nanolattices can be estimated. The three modes to be considered are material fracture, beam buckling, and shell buckling. The critical stress values for each mode are

$$\sigma_{\text{frac}} = \sigma_f, \tag{19}$$

$$\sigma_{\text{buckle}} = \frac{\pi^2 EI}{L_e^2 A_{\text{tube}}}, \tag{20}$$

$$\sigma_{\text{shell}} = \frac{E}{\sqrt{3(1-\nu^2)}} \left(\frac{t}{r_c} \right), \tag{21}$$

respectively. Here, σ_f is the fracture strength, E is the Young's modulus, and ν is the Poisson's ratio of the constituent material. The cross-sectional area of the tube is denoted as A_{tube}, its second area moment is I, and its effective length is L_e (depending on the boundary

conditions). In the case of the octet-truss architecture, $L_e = L/2$, where L is the actual length of the tube. The quantities t and r_c refer to the wall thickness and the wall's radius of curvature, respectively. For a circular hollow tube, $r_c = r$, where r is the tube radius.

Approximating the second area moment to $I = \pi r^3$ and the cross-sectional area to $A_{\text{tube}} = \pi r t$, setting $\sigma_{\text{buckle}} = \sigma_{\text{frac}}$ and $\sigma_{\text{shell}} = \sigma_{\text{frac}}$, and solving for r/l and t/r yields

$$\left(\frac{r}{l}\right)_{\text{crit}} = \frac{1}{2\pi}\sqrt{\frac{\sigma_f}{E}}, \tag{22}$$

$$\left(\frac{t}{r}\right)_{\text{crit}} = \frac{\sigma_f}{E}\sqrt{3(1-\nu^2)}, \tag{23}$$

where $(r/l)_{\text{crit}}$ and $(t/r)_{\text{crit}}$ are the critical ratios below which elastic Euler buckling and elastic shell buckling are expected to dominate over material fracture, respectively.

Supplementary figures

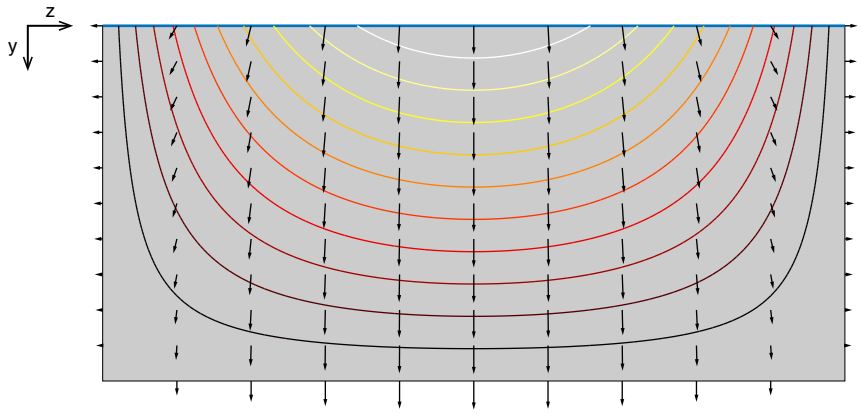

Figure S1: Temperature and heat flux fields calculated from our custom thermal model. This simplified example includes only a single layer. The top boundary is a thin skin of highly conductive material and the left, right, and bottom boundaries are isothermal.

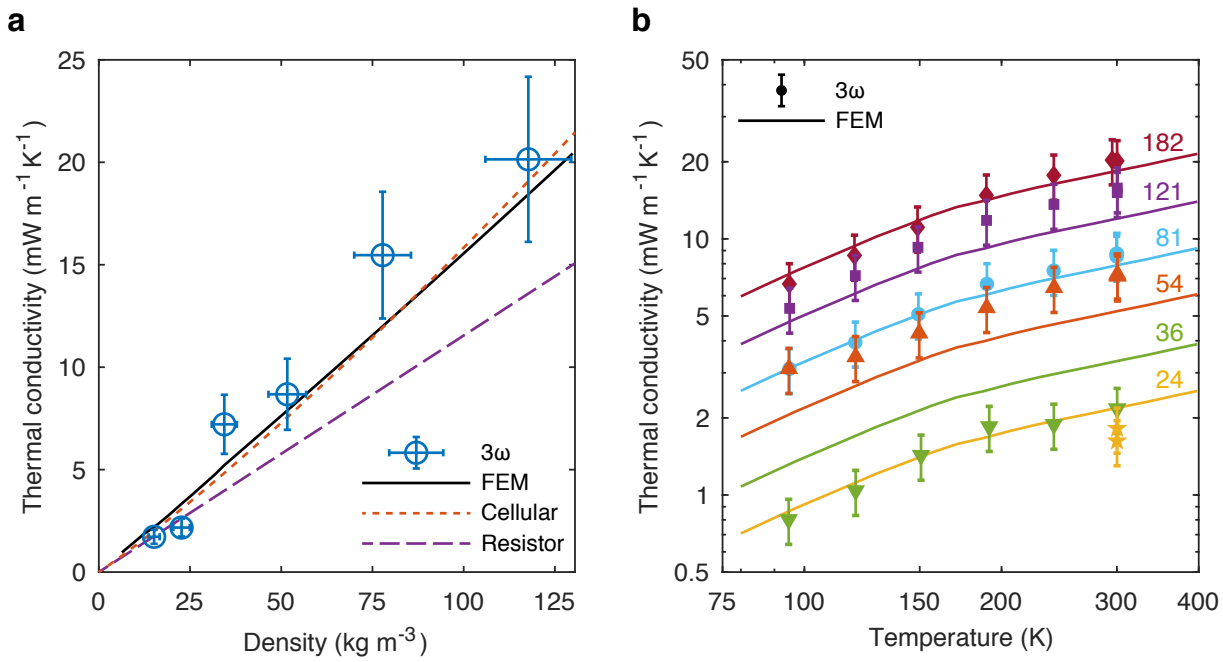

Figure S2: (a) Room temperature thermal conductivity versus density—instead of relative density in Figure 2b—depicting 3ω measurements (symbols), finite element simulations (solid line), a thermal conductivity model developed for cellular solids (dotted line),[11] and our previous thermal resistance model (dashed line).[12] (b) All measured thermal conductivities (symbols) of the six nanolattice samples along with finite element simulation predictions (lines). Data sets are labeled with the wall thickness (nm) above the simulation curve in the same color as the data. Low temperature measurements of the 24 nm sample are not available.

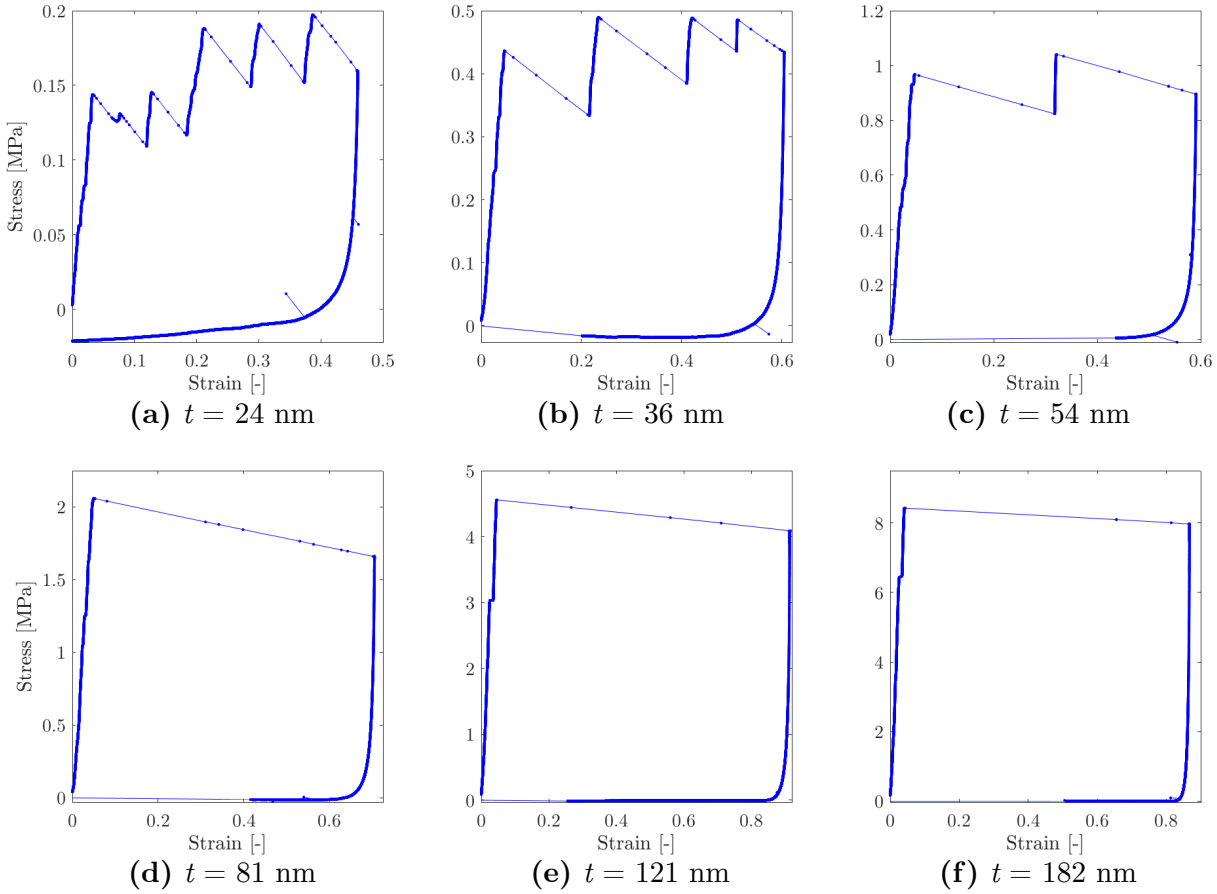

(a) $t = 24$ nm **(b)** $t = 36$ nm **(c)** $t = 54$ nm

(d) $t = 81$ nm **(e)** $t = 121$ nm **(f)** $t = 182$ nm

Figure S3: Representative stress-strain data for compression tests of each nanolattice geometry with varying wall thickness, t.

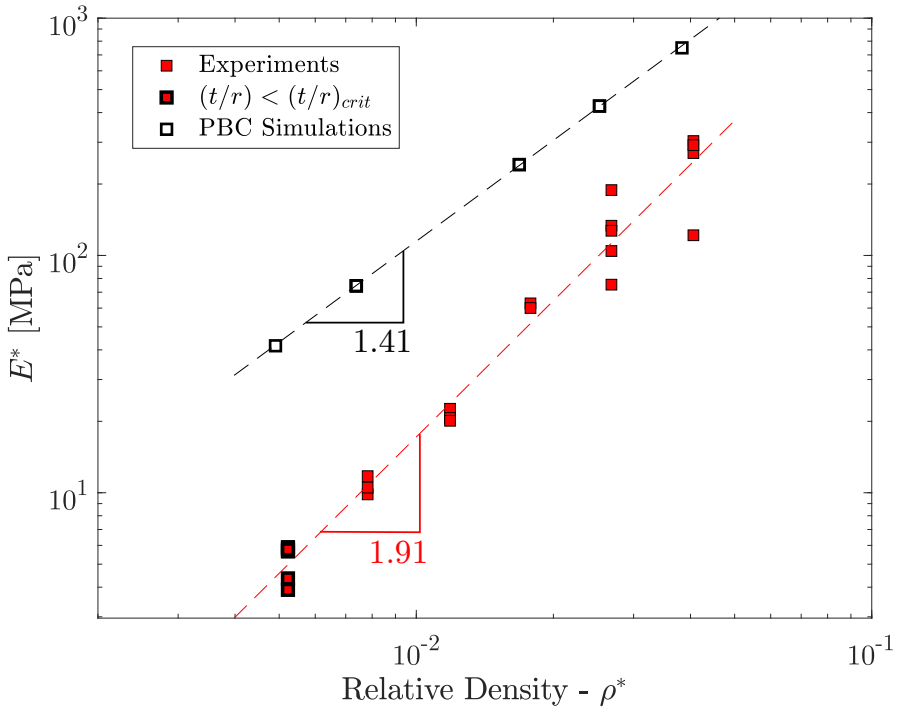

Figure S4: Experimental and computational stiffness values. The experiments where $t/r < (t/r)_{\text{crit}}$ are marked by a thicker black outline. Power-law fits of the form $E^* \propto \rho^m$ for both experiments and simulations are shown as dotted lines.

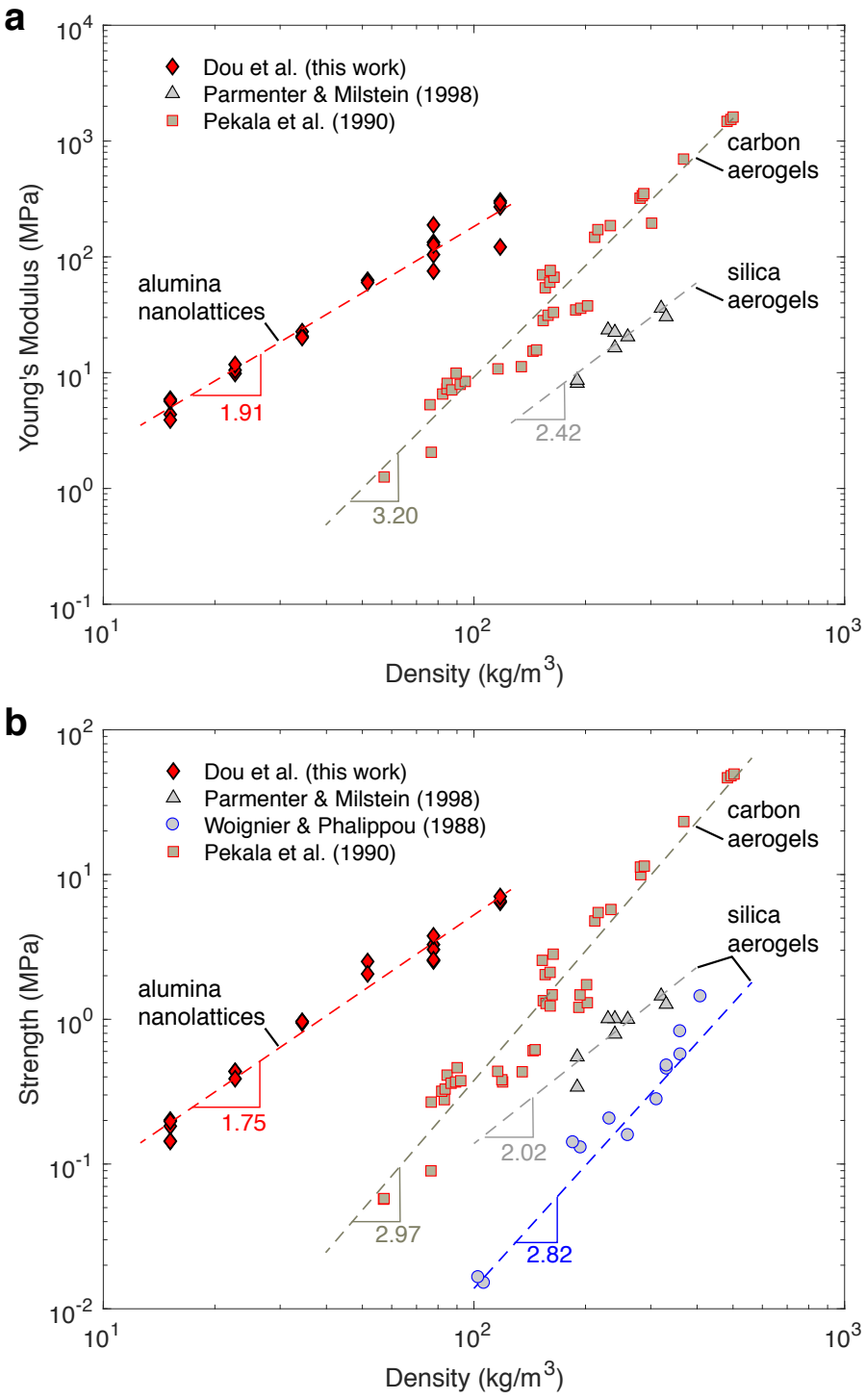

Figure S5: (a) Young's modulus and (b) yield strength versus density of alumina nanolattices in this work compared to silica[13,14] and carbon[15] aerogels.

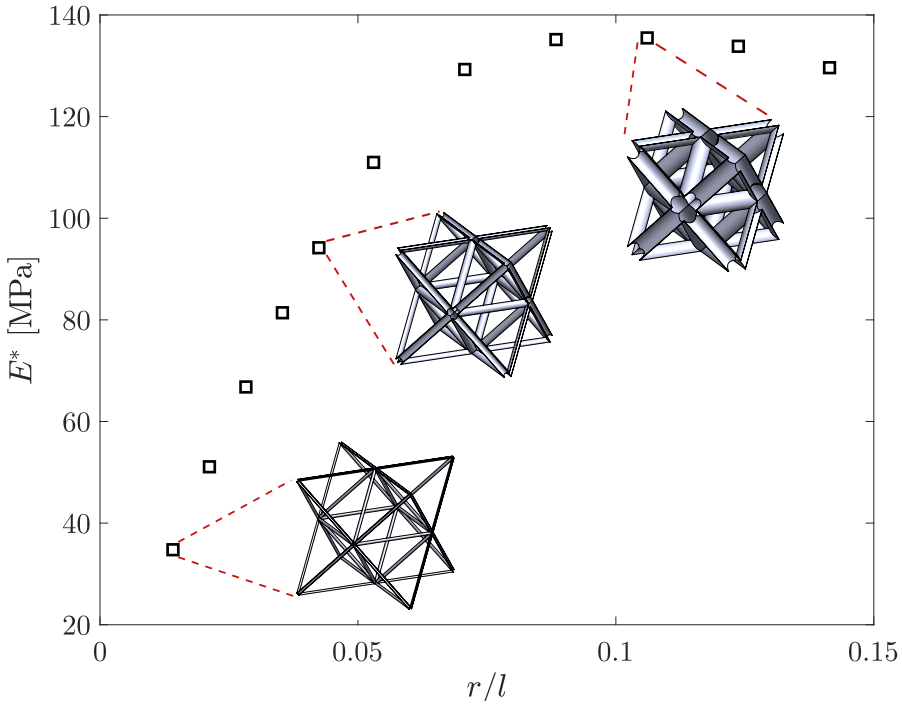

Figure S6: Periodic boundary condition simulations with a constant wall thickness but varying r/l, showing optimal values of r/l to maximize stiffness.

References

(1) Meza, L. R.; Das, S.; Greer, J. R. Strong, lightweight, and recoverable three-dimensional ceramic nanolattices. *Science* **2014**, *345*, 1322–1326.

(2) Touloukian, Y. S.; Powell, R. W.; Ho, C. Y.; Klemens, P. G. *Thermophysical Properties of Matter—The TPRC Data Series*; IFI/Plenum Data Corporation: New York, 1970.

(3) Groner, M. D.; Fabreguette, F. H.; Elam, J. W.; George, S. M. Low-Temperature Al_2O_3 Atomic Layer Deposition. *Chem. Mater.* **2004**, *16*, 639–645.

(4) Lee, S.-M.; Cahill, D. G.; Allen, T. H. Thermal conductivity of sputtered oxide films. *Phys. Rev. B: Condens. Matter Mater. Phys.* **1995**, *52*, 253–257.

(5) Kahlbaum, G. W. A.; Roth, K.; Siedler, P. Über Metalldestillation und über destillierte Metalle. *Zeitschrift für anorganische Chemie* **1902**, *29*, 177–294.

(6) Berdova, M.; Ylitalo, T.; Kassamakov, I.; Heino, J.; Törmä, P. T.; Kilpi, L.; Ronkainen, H.; Koskinen, J.; Hæggström, E.; Franssila, S. Mechanical assessment of suspended ALD thin films by bulge and shaft-loading techniques. *Acta Mater.* **2014**, *66*, 370–377.

(7) Meza, L. R.; Phlipot, G. P.; Portela, C. M.; Maggi, A.; Montemayor, L. C.; Comella, A.; Kochmann, D. M.; Greer, J. R. Reexamining the mechanical property space of three-dimensional lattice architectures. *Acta Mater.* **2017**, *140*, 424–432.

(8) Ma, J.; Parajuli, B. R.; Ghossoub, M. G.; Mihi, A.; Sadhu, J.; Braun, P. V.; Sinha, S. Coherent Phonon-Grain Boundary Scattering in Silicon Inverse Opals. *Nano Lett.* **2013**, *13*, 618–624.

(9) Carslaw, H. S.; Jaeger, J. C. *Conduction of Heat in Solids*, 2nd ed.; Oxford University Press: Oxford, 1986.

(10) Borca-Tasciuc, T.; Kumar, A. R.; Chen, G. Data reduction in 3ω method for thin-film thermal conductivity determination. *Rev. Sci. Instrum.* **2001**, *72*, 2139–2147.

(11) Ashby, M. F. The properties of foams and lattices. *Philos. Trans. R. Soc. A* **2006**, *364*, 15–30.

(12) Dou, N. G.; Minnich, A. J. Heat conduction in multifunctional nanotrusses studied using Boltzmann transport equation. *Appl. Phys. Lett.* **2016**, *108*, 011902.

(13) Parmenter, K. E.; Milstein, F. Mechanical properties of silica aerogels. *J. Non-Cryst. Solids* **1998**, *223*, 179–189.

(14) Woignier, T.; Phalippou, J. Mechanical strength of silica aerogels. *J. Non-Cryst. Solids* **1988**, *100*, 404–408.

(15) Pekala, R. W.; Alviso, C. T.; LeMay, J. D. Organic aerogels: microstructural dependence of mechanical properties in compression. *J. Non-Cryst. Solids* **1990**, *125*, 67–75.